

Quantum-enabled Rydberg atomic polarimetry of radio-frequency fields

Matthew Cloutman¹,¹ Matthew Chilcott¹,¹ Alexander Elliott,²
J. Susanne Otto¹,¹ Amita B. Deb³,³ and Niels Kjærgaard¹,^{*}

¹*Department of Physics, QSO-Quantum Science Otago,
and Dodd-Walls Centre for Photonic and Quantum Technologies,
University of Otago, Dunedin 9016, New Zealand*

²*Department of Physics and Dodd-Walls Centre for Photonic and Quantum Technologies, University of Auckland, New Zealand*

³*School of Physics and Astronomy, University of Birmingham,
Edgbaston, Birmingham B15 2TT, United Kingdom*

(Dated: March 25, 2025)

Rydberg atoms efficiently link photons between the radio-frequency (RF) and optical domains. They furnish a medium in which the presence of an RF field imprints on the transmission of a probe laser beam by altering the coherent coupling between atomic quantum states. The immutable atomic energy structure underpins quantum-metrological RF field measurements and has driven intensive efforts to realize inherently self-calibrated sensing devices. Here we investigate spectroscopic signatures owing to the angular momentum quantization of the atomic states utilized in an electromagnetically-induced transparency (EIT) sensing scheme for linearly-polarized RF fields. Specific combinations of atomic terms are shown to give rise to universal, distinctive fingerprints in the detected optical fields upon rotating the RF field polarization. Using a dressed state picture, we identify two types of angular momentum ladders that display strikingly disparate spectroscopic signatures, including the absence or presence of a central spectral EIT peak. We verify our predicted complementary response in rubidium vapour cell experiments and through density matrix calculations. Our study adds important insights into the prospects of Rydberg atomic polarimetry for quantum metrological electric field characterization.

Since the turn of the millennium, Rydberg atoms have experienced a veritable renaissance, emerging as a workhorse for quantum-technological applications¹. Prompted by the proposal to exploit their long range dipolar interactions for quantum-computational gate operations², extensive efforts were devoted to making Rydberg atomic quantum information processors a reality³. Along another avenue, Rydberg atoms found themselves at the heart of vapor-based sensing applications^{4–8} following the seminal 2012 work by Sedlacek et al.⁹

Unlike Rydberg-based quantum computers and simulators which require laser cooled atoms in an elaborate ultrahigh vacuum setup, Rydberg sensing can be achieved with simple, sealed glass cells. The cells contain a room-temperature gas of alkali atoms to form a transducer ‘wired up’ with laser beams to read out measurements^{10,11}. These sensors capitalize on the spectacular magnitude of electric transition dipole-moments between Rydberg excited states to accurately determine the amplitudes of RF electric fields with frequencies extending into the THz domain. Moreover, because such measurements can be tied to transitions between quantum states of an atom, Rydberg-atomic schemes establish an inherently self-calibrated RF-field probe^{12,13}. The obvious metrological advantage of self-calibrated, SI-traceable atomic probes over conventional, metallic dipole antennas has triggered a worldwide surge in experiments devoted to vapour-based RF-field sensing^{6,13–17}.

Rydberg-atomic vapour-cell sensing offers unique capabilities for measuring polarized RF-fields. For example, an isotropic response to a linearly-polarized field is fundamentally prohibited for a conventional electric receiver antenna^{18–20}. In contrast, by employing properly selected quantum states of a Rydberg atomic system it may realise an ideal isotropic receiver^{10,21–23}. Alternatively, quantum states can be selected to achieve a polarization-dependent response that enables atom-based RF vector electrometry^{24–27}.

In this study, we demonstrate a Rydberg electrometer operating in two modes with diametrically opposed polarization-dependent spectroscopic responses. The complementary response is engineered through a judicious choice of the atomic angular momentum structure in play for each mode. In particular, we identify two types of quantum-state ladders that give rise to out-of-phase oscillatory signals as the angle of a linearly-polarized RF field is scanned akin to the action of an optical polarizing beam splitter. The complementary responses of the ‘output ports’ are modelled well by density matrix calculations and open up important prospects for polarimetric antenna characterisation with atom-based sensors²⁸.

Results

Polarization dependent RF sensing in Rydberg EIT—a conceptual model

To set the scene, we introduce in Fig. 1a the energy level diagram for a fictitious four-level model atom that includes angular momentum degeneracy for the ground and second excited levels. A probe laser field linearly polarized along the z -axis matches the optical transition

* niels.kjaergaard@otago.ac.nz

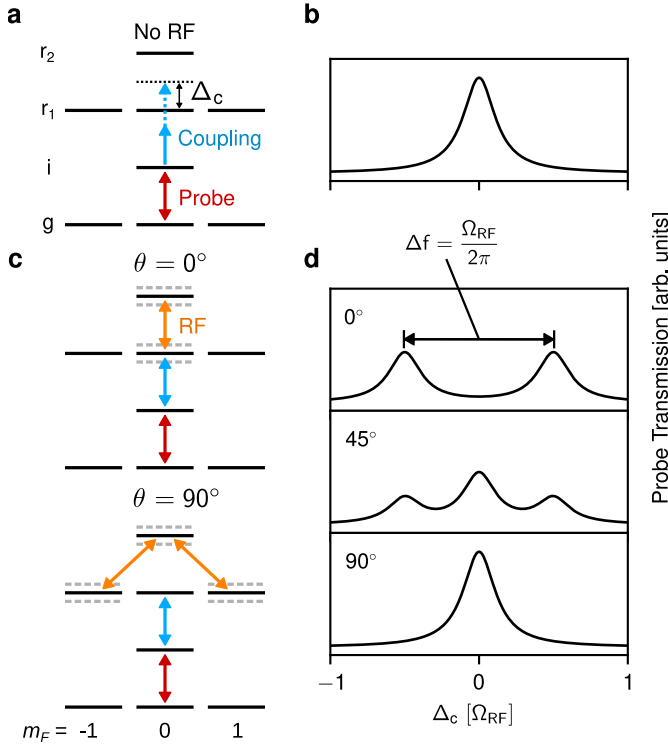


Fig. 1 | **a** Level diagram of a four-level model atom with three-fold degeneracy of its ground (g) and second excited level (r_1). A linearly-polarised probe field is resonant with the transition from g to the first excited level i . A coupling field has a frequency close to the transition from i to r_1 , giving rise to an EIT peak for the transmitted probe field when its detuning Δ_c is scanned (**b**). **c** The model atom dressed in an RF-field that is parallelly ($\theta = 0^\circ$) or perpendicularly ($\theta = 90^\circ$) polarized with respect to the optical probe and coupling fields. The resulting AT splitting is shown indicated with dashed lines. **d** Simulated probe transmission spectra for $\theta = 0^\circ$, 45° , and 90° . Ω_{RF} denotes the Rabi frequency characterizing the RF coupling.

frequency between the ground level g and an excited level i ; choosing \hat{z} as the quantization axis for the model atom, the probe field can drive a π -transition between $|g, m = 0\rangle$ (one of three degenerate angular momentum states of the ground level) and $|i, m = 0\rangle$.

An optical probe beam interacting resonantly with a collection of model atoms on the $g \leftrightarrow i$ -transition will be attenuated as light is scattered out of the probe mode. However, by adding an additional laser field that couples the excited level i resonantly to a third level r_1 , the atomic medium can be made transparent to the probe laser beam through the mechanism of electromagnetically induced transparency (EIT)²⁹. For our model atom, the excited intermediate state $|i, m = 0\rangle$ connects with a higher-lying state $|r_1, m = 0\rangle$ (one of three degenerate angular momentum states of the Rydberg level r_1) through an optical coupling field that is linearly co-polarized with the probe field along \hat{z} . Because of the ascending energies of the levels involved, the resulting EIT for the probe

field is referred to as a ladder scheme. The EIT transmission is maximised for a coupling field detuning $\Delta_c = 0$ as illustrated in Fig. 1b.

We next consider the effect of adding a linearly-polarized RF field to our model atom that resonantly couples the Rydberg level r_1 to another Rydberg level r_2 . It is unimportant if r_2 lies above or below r_1 in energy and without loss of generality we will depict it above r_1 (see Fig. 1a). For the RF field polarization aligned at an angle $\theta = 0^\circ$ with respect to the optical fields, the non-degenerate state $|r_2, m = 0\rangle$ connects to $|r_1, m = 0\rangle$, the top rung of the EIT ladder. The RF coupling $|r_2, m = 0\rangle \leftrightarrow |r_1, m = 0\rangle$ acts to disrupt the optical EIT for $\Delta_c = 0$ through the Autler-Townes (AT) effect³⁰. For $\theta = 90^\circ$, the $|r_1, m = 0\rangle$ top rung of the EIT ladder is left unconnected by the RF-field and EIT proceeds exactly as if the RF field had not been present. Figure 1c shows level diagrams and the coupled states for the two cases $\theta = 0^\circ, 90^\circ$; the state-splitting resulting from the coupling is indicated with dashed lines. Figure 1d displays the associated calculated EIT spectra of the optical probe transmission versus the coupling laser field detuning Δ_c which is double peaked (AT doublet) for $\theta = 0^\circ$ and single peaked for $\theta = 90^\circ$. Also shown is the triple peaked spectrum found at $\theta = 45^\circ$ (all spectra for angles between $\theta = 0^\circ$ and $\theta = 90^\circ$ will have three peaks, with the central-to-sidelobe ratio increasing with θ).

Rydberg atomic RF-polarimetry in a complex multi-level atom

The simple EIT-probed model-atom level structure of Fig. 1 displays two salient features when a linearly-polarized RF field is added. For the polarization $\theta = 0^\circ$, an AT doublet is encountered in the spectrum due to a vertical, pure $m = 0$ four-level ladder, while for $\theta = 90^\circ$ we have a pure three-level system and a single central EIT peak. As such, the EIT spectrum carries an imprint of the polarization state of the RF field. A similar polarization dependence will generally be encountered for real atoms with a more complex level structure and this opens up the prospect of atomic RF polarimetry. Its utilization, however, necessitates a detailed understanding of the polarization signature resulting from a particular atomic level structure.

Figure 2a reproduces the essence of Fig. 1(a) of Ref. 24, that considered the $5S_{1/2}^{F=2} \leftrightarrow 5P_{3/2}^{F=3} \leftrightarrow 53D_{5/2} \leftrightarrow 54P_{3/2}$ ladder of ^{87}Rb as a tool for vector electrometry. The hyperfine sub-levels (F -levels) of the $53D_{5/2}$ level and the upper $54P_{3/2}$ are unresolved, so to enable a visual tracking of all dipole-allowed transitions in the diagram, relative vertical offsets ($\propto F$) have been added to the Rydberg sub-states.³¹ The red crosses serve to illustrate that an RF field polarized along the chosen quantization axis does not directly connect the stretched states $D_{5/2}(F = 4, m_F = \pm 4)$ to the upper $P_{3/2}$ Rydberg level. Reference 24 points out that the system when probed with optical fields polarized perpendicularly to the RF

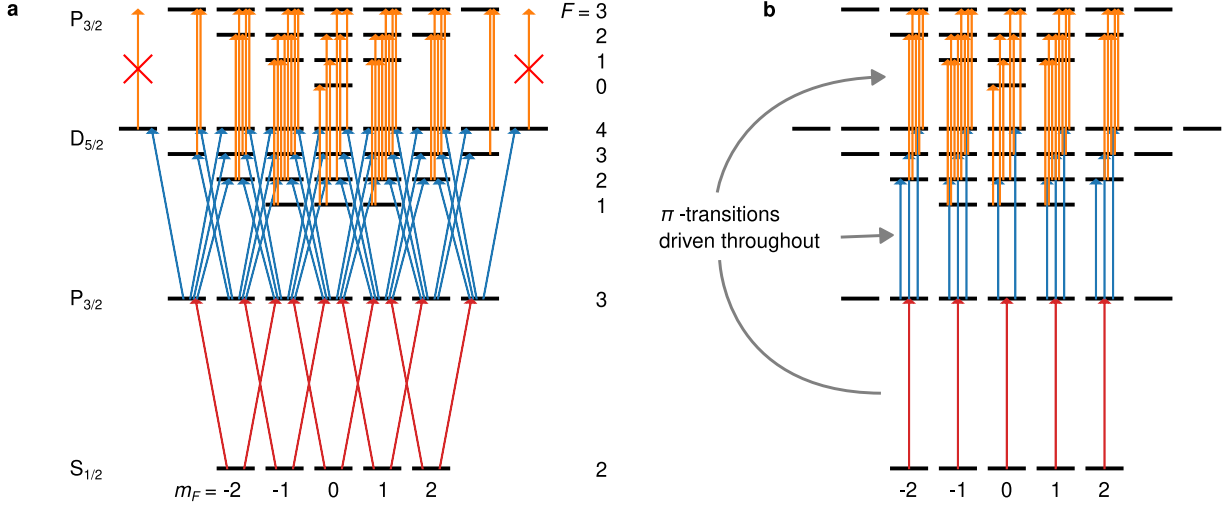


Fig. 2 | Hyperfine level diagrams for the $S_{1/2}^{F=2} \leftrightarrow P_{3/2}^{F=3} \leftrightarrow D_{5/2} \leftrightarrow P_{3/2}$ excitation ladder with the ultimate and penultimate levels (Rydberg levels) resonantly coupled by an RF field, which is linearly polarized along the atomic quantization axis and drives π -transitions (orange arrows). Red and blue arrows shows the allowed transitions for optical probe and coupling fields linear polarized perpendicularly to the RF field (a, optical σ -transitions) and parallel to the RF field (b, optical π -transitions). The F -levels for the Rydberg states are energetically degenerate, and have been offset vertically to illustrate the dipole-allowed transitions in play.

field—the situation encountered in Fig. 2a—therefore presents three-level EIT excitation pathways [specifically, $S(F=2, m_F=\pm 2) \rightarrow P(F=3, m_F=\pm 3) \rightarrow D(F=4, m_F=\pm 4)$]. Reference 32 reiterates this point, noting that the $D_{5/2}(F=4, m_F=\pm 4)$ states are “unsplit” by the RF field. The EIT spectrum for crossed RF and optical polarizations ($\theta = 90^\circ$) will hence include a central peak at zero detuning as either the probe or coupling field is scanned.

The scenario of parallel RF and optical polarizations is captured in Fig. 2b. Here Ref. 24 argues that “In this case, π transitions are driven throughout the system and all excitation pathways experience a four level system. The theoretical and experimental spectra have two transmission peaks...”. While the experiments of Ref. 24 were compatible with two EIT transmission peaks for $\theta = 0^\circ$, theory will, as we shall see, in fact predict four transmission peaks for a $S_{1/2}^{F=2} \leftrightarrow P_{3/2}^{F=3} \leftrightarrow D_{5/2} \leftrightarrow P_{3/2}$ ladder system; the reason that a four-peaked spectrum is not observed in Ref. 24 is because insufficient RF power is applied to resolve the structure. But perhaps more importantly, the absence of a central transmission peak is *not* the result of π -transitions being driven throughout the system. As a case in point, we will contrast the $S_{1/2}^{F=2} \leftrightarrow P_{3/2}^{F=3} \leftrightarrow D_{5/2} \leftrightarrow P_{3/2}$ system to that of $S_{1/2}^{F=2} \leftrightarrow P_{3/2}^{F=3} \leftrightarrow D_{3/2} \leftrightarrow P_{1/2}$. Figure 3 shows a level diagram of the latter with transitions for co-polarized RF and optical fields. Similarly to the $S_{1/2}^{F=2} \leftrightarrow P_{3/2}^{F=3} \leftrightarrow D_{5/2} \leftrightarrow P_{3/2}$ system in Fig. 2b, only π -transitions are driven throughout the system, yet, as we shall demonstrate, the $S_{1/2}^{F=2} \leftrightarrow P_{3/2}^{F=3} \leftrightarrow D_{3/2} \leftrightarrow P_{1/2}$ system displays a dominant central transmission peak for $\theta = 0^\circ$. In fact, the central transmission peak encountered at $\theta = 0^\circ$

dwarfs the central peak at $\theta = 90^\circ$.

Criterion for a central EIT peak

To seek the origin of the absent central EIT peak of the

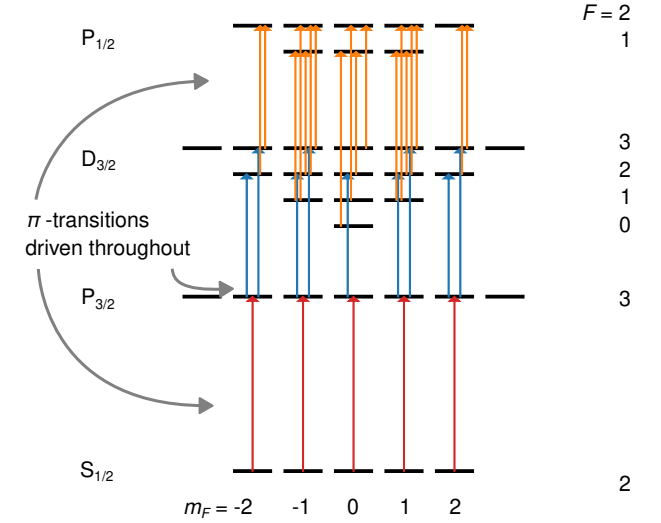


Fig. 3 | Hyperfine level diagrams for the $S_{1/2}^{F=2} \leftrightarrow P_{3/2}^{F=3} \leftrightarrow D_{3/2} \leftrightarrow P_{1/2}$ excitation ladder with the ultimate and penultimate levels (Rydberg levels) resonantly coupled (orange arrows) by an RF field, which is linearly polarized along the atomic quantization axis. Optical coupling (blue arrows) and probe (red arrows) fields are also linearly polarized along the quantization axis and π -transitions are driven throughout the system.

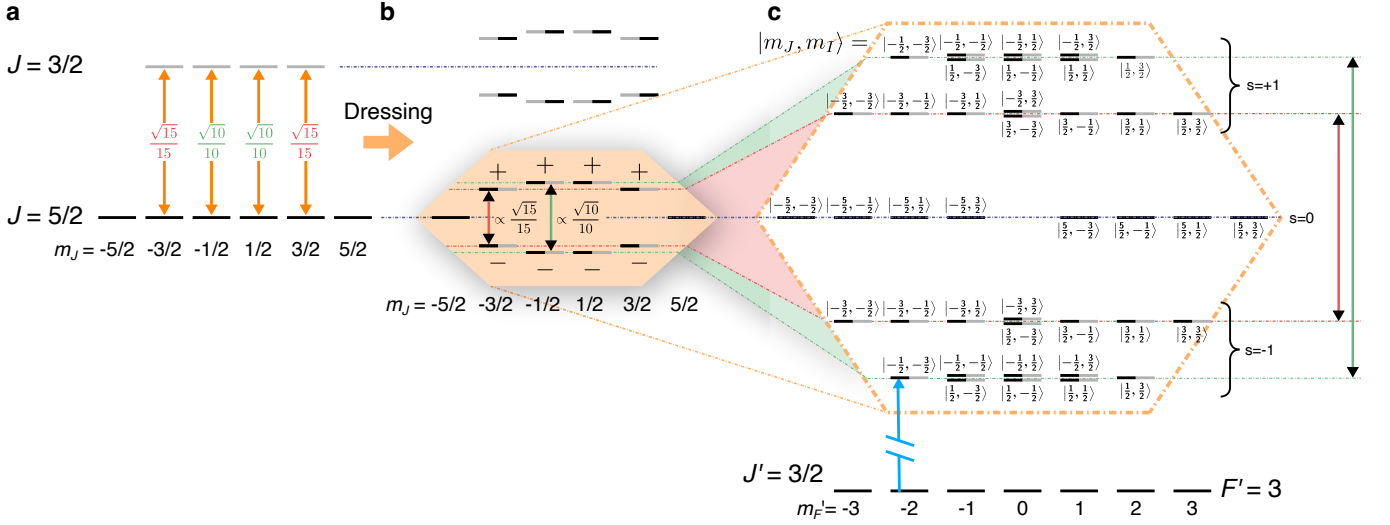


Fig. 4 | RF-dressed Rydberg levels—procedure for finding the energy structure probed by EIT. **a** A linearly-polarized RF field couples states of lower ($J = 5/2$, black) and upper ($J = 3/2$, grey) Rydberg levels via π -transitions with dipole matrix elements as indicated. **b** Field-dressed Rydberg levels with m_J -dependent AT-splitting. Each grey-black state in the diagram represents an equal two-component superposition of $J = 5/2$ and $J = 3/2$ states with the adjacent \pm indicating its symmetry. **c** Labelling the lower dressed manifold of **b** to include all possible values for the nuclear spin projection m_I so that each state inside the hexagon is designated by $|m_J, m_I\rangle$ (and hence $m_F = m_J + m_I$) as well as a symmetry parameter s . Each $|m_J, m_I; s\rangle$ can be expanded using (1) which facilitates the evaluation of the transition strength for the optical coupling from a state $|J' = 3/2, F' = 3, m'_F = m_F\rangle$ through (2).

system of Fig. 2b

$$\underbrace{S_{1/2}^{F=2}}_g \leftrightarrow \underbrace{P_{3/2}^{F=3}}_i \leftrightarrow \underbrace{D_{5/2}}_{r_1} \leftrightarrow \underbrace{P_{3/2}}_{r_2}, \quad (\text{I})$$

we first consider, in isolation, the two Rydberg levels r_1 and r_2 at energies ϵ_{r_1} and ϵ_{r_2} , respectively, dressed by a resonant linearly-polarized RF field with angular frequency $\omega_{\text{RF}} = |\epsilon_{r_2} - \epsilon_{r_1}|/\hbar$. As mentioned above, hyperfine structure is completely negligible for the Rydberg levels and this part of the problem can therefore be

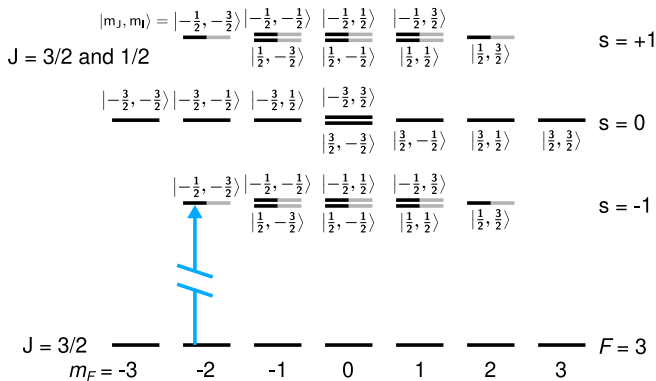


Fig. 5 | Diagram for evaluating the optical coupling from a state $|J' = 3/2, F' = 3, m'_F = m_F\rangle$ to a state in a field-dressed $D_{3/2} \leftrightarrow P_{1/2}$ Rydberg manifold. The procedure for obtaining this diagram follows that of Fig. 4 and each of the states $|m_J, m_I; s\rangle$ can be expanded using (1).

treated in a fine-structure basis where it separates into a series of individual, driven two-level systems and two uncoupled r_1 spectator states ($m_J = \pm 5/2$). The Rabi frequency for each two level system depends on $|m_J|$ and varies as indicated in Fig. 4a. As a result of the resonant RF coupling, the AT effect leads to varying splittings across the lower r_1 -level as shown in Fig. 4b. The energy spectrum ϵ_{r_1} now has five peaks where, for the bare atom, there was only one—this results directly from the $\uparrow J_{1=5/2}$ -level structure³³.

Unlike the Rydberg levels r_1 and r_2 , the g and i levels display resolvable hyperfine structure, and excitation to r_1 specifically departs from the $F = 3$ i -level. It is important to note that because of Laporte's rule, an i -level state cannot couple to the r_2 component of a dressed state because the change in orbital angular momentum between i and r_2 will differ from unity (for our experiments both are described by P -terms). Hence we will exclusively be concerned with the transitions from states $|F = 3, m_F = -3\rangle \dots |F = 3, m_F = 3\rangle$ of the i -level to the r_1 components of the dressed manifold centred on ϵ_{r_1} .

To establish how the RF field dressing of the atom affects the optical EIT probing we transform to a hyperfine basis, where J is coupled to the spin of the atomic nucleus $I = 3/2$ to form $F = J + I$. Figure 4c recasts the lower dressed manifold of Fig. 4b (orange hexagon) to include the possible projections m_I of the nuclear spin. In doing so, each state of Fig. 4c is designated by quantum numbers m_J and m_I in addition to a parameter $s = 0, \pm 1$ that tracks the symmetry of the parental dressed state of

Figure 4b from which it descends: every dressed state in Fig. 4b is either an equal symmetric ($s = +1$) or antisymmetric ($s = -1$) superposition of r_1 and r_2 components. The r_1 spectator states that are unaffected by the dressing field ($m_J = \pm 5/2$) are labeled by $s = 0$. Expanding the r_1 part (i.e., $J = 5/2$) of each state of Fig. 4c as

$$|m_J m_I; s\rangle = \left[\frac{1}{\sqrt{2}} \right]^{1/2} \sum_{F=1}^4 \underbrace{\langle J I F m_F | J m_J I m_I \rangle}_{C_{J m_J I m_I}^{F m_F}} |F m_F\rangle, \quad (1)$$

we obtain the required transformation to the hyperfine basis. A measure for the strength of an optical π -transition from a particular state $|J' F' m'_F\rangle$ of the i -level (i.e., $J' = 3/2$) to a state of the lower dressed Rydberg manifold can now be found (see Supplementary Note 1):

$$\begin{aligned} & |\langle J' F' m'_F | -e r_0 | J m_J I m_I; s \rangle|^2 \\ &= \frac{1}{2^{|s|}} e^2 \left| \sum_{F=1}^4 C_{J m_J I m_I}^{F m_F} \langle F' m'_F | r_0 | F m_F \rangle \right|^2 \\ &\propto 2^{-|s|} \left(\begin{matrix} J' & J & 1 \\ -m_J & m_J & 0 \end{matrix} \right)^2 \left(\begin{matrix} J' & F' & I \\ -m_J & m'_F & m_J - m'_F \end{matrix} \right)^2 \quad (2) \end{aligned}$$

The first 3- j symbol of (2) vanishes if $|m_J| > J'$. An optical field co-polarized with the linear RF dressing field can therefore not couple any of states of the $P_{J'=3/2}$ i -level manifold to the dressed Rydberg states with $m_J = \pm 5/2$. The EIT spectrum will hence not display a central peak.

Using the $S_{1/2}^{F=2} \leftrightarrow P_{3/2}^{F=3} \leftrightarrow D_{5/2} \leftrightarrow P_{3/2}$ system (type-I ladder) as an illustration, we have shown that, generally, for co-polarized fields the EIT spectrum will not have a central peak if $J_{r_1} > J_i$. Furthermore, an obvious requirement for a central peak is $J_{r_1} > J_{r_2}$ —the r_1 -level needs to have spectator states. An equivalent analysis of the superficially similar system

$$\underbrace{S_{1/2}^{F=2}}_g \leftrightarrow \underbrace{P_{3/2}^{F=3}}_i \leftrightarrow \underbrace{D_{3/2}}_{r_1} \leftrightarrow \underbrace{P_{1/2}}_{r_2}, \quad (II)$$

presented in Fig. 3 yields the dressed level diagram shown in Fig. 5. When, for this type-II ladder, we consider the dipole matrix elements for optical π -transitions from the i -level to the Rydberg manifold, we see that $|m_J| = \{\frac{1}{2}, \frac{3}{2}\} \leq J' = \frac{3}{2}$. We do therefore not experience the vanishing of first 3- j symbol in (2). Rather, its common, non-zero squared magnitude

$$\left(\begin{matrix} J' & J & 1 \\ -m_J & m_J & 0 \end{matrix} \right)^2 \propto m_J^2 \quad (3)$$

for the central $m_J = \pm 3/2$ -states is ninefold that of the split $m_J = \pm 1/2$ states. Hence, despite the fact “ π transitions are driven throughout the system”, a double peak structure is *not* predicted, but instead a triple peak spectrum with a strong central peak.

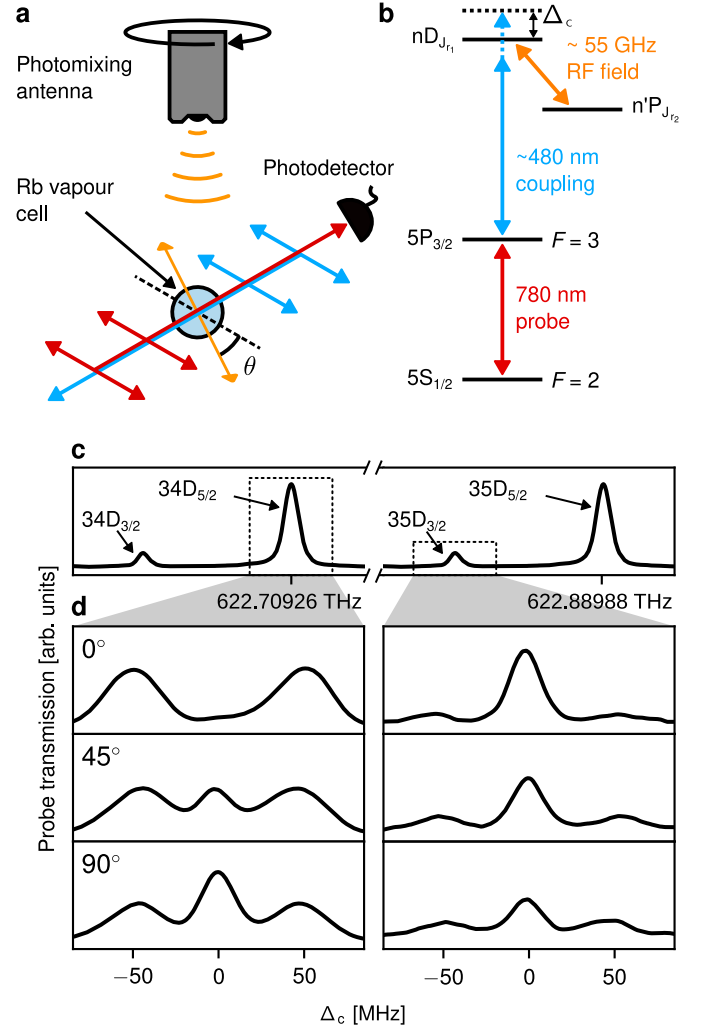


Fig. 6 | **a** Schematic of experimental setup. Probe and coupling lasers are linearly polarized in the horizontal plane and counter-propagate through a spherical Rb vapour cell. A photomixing antenna mounted in a motorized rotation stage emits linearly-polarized RF radiation along a vertical direction. **b** Atomic level structure for ^{87}Rb applicable to both type-I and type-II ladders. **c** Probe transmission spectra showing EIT peaks when the coupling laser frequency is scanned. **d** Probe transmission spectra when resonant RF-radiation is applied to the $34D_{5/2} \leftrightarrow 35P_{3/2}$ (left column) and $35D_{3/2} \leftrightarrow 36P_{1/2}$ (right column) transitions as a function of the coupling laser detuning Δ_c ; spectra for $\theta = 0^\circ, \theta = 45^\circ, 90^\circ$ are shown.

Experiment

To verify the predicted complementarity in the polarization response of the two types of ladders encountered above, we perform optical EIT spectroscopy on the $5S_{1/2}^{F=2} \leftrightarrow 5P_{3/2}^{F=3} \leftrightarrow 34D_{5/2} \leftrightarrow 35P_{3/2}$ (type-I) and $5S_{1/2}^{F=2} \leftrightarrow 5P_{3/2}^{F=3} \leftrightarrow 35D_{3/2} \leftrightarrow 36P_{1/2}$ (type-II) ladders of ^{87}Rb .

Figure 6a shows a schematic of our experimental setup. Using a photodetector, we measure the transmission of a

780 nm probe laser beam, propagating along a horizontal axis through a centimeter-sized borosilicate glass cell containing a room temperature rubidium vapour. The frequency of the probe laser is fixed and resonant with the $5S_{1/2}^{F=2} \leftrightarrow 5P_{3/2}^{F=3}$ D2 line of ^{87}Rb (see Fig. 6b). A counter propagating $\sim 480\text{ nm}$ coupling laser is scanning in frequency across the transitions from $5P_{3/2}$ ($F=3$) to either $34D_{5/2}$ (type-I ladder) or $35D_{3/2}$ (type-II ladder).

Figure 6c shows the transmitted probe light for a frequency scan of the coupling light over the two transitions we utilize for RF-sensing (see Methods). Both probe and coupling beams are linearly polarized in the horizontal plane. A photomixing antenna (see Methods) emits linearly-polarized $\sim 55\text{ GHz}$ RF-radiation down onto the vapour cell along a (nominally) vertical axis intersecting the horizontally propagating optical beams. At the point of intersection, the angle between polarizations of the RF field and the optical fields is θ (see Figure 6a). We can vary this angle by rotating the photoconductive antenna about its axis.

Figure 6d shows EIT spectra acquired for the resonantly driven $34D_{5/2} \leftrightarrow 35P_{3/2}$ (left panel, type-I ladder) and $35D_{3/2} \leftrightarrow 36P_{1/2}$ (right panel, type-II ladder) Rydberg transitions, for $\theta = 0^\circ$, 45° , and 90° . The polarization signatures for the type-I ladder in the left panel are similar to those reported for the $53D_{5/2} \leftrightarrow 54P_{3/2}$ Rydberg transition in Ref. 24. In particular, for $\theta = 0^\circ$ we note the absence of a central peak and what appears to be an AT doublet. The above dressed-picture analysis of the system predicted a five peak spectrum with no central component (an effective four peak spectrum) at $\theta = 0^\circ$. The differential splitting of the Doppler broadened $m_J = \pm 3/2$ and $m_J = \pm 5/2$ lines is however too small at our applied RF power to be resolved. Rotating the emitter to $\theta = 90^\circ$, we observe, again in correspondence with Ref. 24, how the heights of the split peaks reduce while a prominent central peak emerges at $\Delta_c = 0$. Also for this situation, each of the split peaks in fact contains two spectral features that are obscured by broadening.

Comparing the EIT spectra of the RF-dressed $5S_{1/2}^{F=2} \leftrightarrow 5P_{3/2}^{F=3} \leftrightarrow 34D_{5/2} \leftrightarrow 35P_{3/2}$ type-I ladder to that of $5S_{1/2}^{F=2} \leftrightarrow 5P_{3/2}^{F=3} \leftrightarrow 35D_{3/2} \leftrightarrow 36P_{1/2}$ type-II ladder, we find a compelling difference. In particular, for the type-II case and $\theta = 0^\circ$, where “ π -transitions are driven throughout the system”, we observe a prominent central peak at $\Delta_c = 0$ (cf. Fig. 6d). Moreover, in contrast to the $5S_{1/2}^{F=2} \leftrightarrow 5P_{3/2}^{F=3} \leftrightarrow 34D_{5/2} \leftrightarrow 35P_{3/2}$ ladder, the central peak is minimized at $\theta = 90^\circ$.

The complementarity in spectral behaviour for type-I and type-II ladders is elucidated further in the ‘spectrograms’ of Fig. 7, representing the sequentially recorded EIT spectra when rotating the RF-emitter in 5° increments for a full 360° revolution. The left and the right columns compare the type-I and -II cases as the power of the resonant RF dressing field is varied through the applied bias voltage to the photomixing antenna V_{Bias} .

In both cases we see an evolution where the $\Delta_c = 0$ EIT peak in the absences of an RF field (horizontal line features in the top row) progressively ‘breaks up’ as the RF increases. The breakup, however, happens in a complementary fashion with the type-I ladder developing transmission minima and maxima at the (θ, Δ_c) -coordinates where the type-II ladder presents its respective maxima and minima. This happens along the line $\Delta_c = 0$ for which Fig. 7b shows their out-of-phase π -periodic undulations.

Numerical Simulations

The transmitted probe laser intensity I in the spectrograms of Fig. 7 are described by Beer-Lambert’s law

$$I(\theta, \Delta_c) = I_0 e^{-\alpha(\theta, \Delta_c)\ell}, \quad (4)$$

where I_0 is the intensity of the probe light before traversing the distance ℓ through the vapour. The extinction coefficient α is proportional to a weighted sum over the off-diagonal elements of the density matrix that involves the combination of g and i -states [See (S6) of Supplementary Note 2]. To simulate the variation of $\alpha(\theta, \Delta_c)$ over a spectrogram for a given RF dressing power, we therefore calculate the steady-state atomic density matrix under the combined influence of the optical and RF fields (see Methods). The density matrix for each case includes all individual $|Fm_F\rangle$ hyperfine states of the ladder levels (cf. Fig. 2 and Fig. 3). For the type-I ladder of Fig. 2 involving a $D_{5/2} \leftrightarrow P_{3/2}$ Rydberg transition, this amounts to 52 atomic states, whereas the type-II ladder of Fig. 3 capped by the $35D_{3/2} \leftrightarrow 36P_{1/2}$ transition requires 36 atomic states. As in Ref. 34 an auxiliary “dummy state” is included to incorporate effective incoherent decay from transit-time broadening, collisions, and radiative decay from the Rydberg states. In our simulations, the RF power is the only fitted quantity with all other input parameters such as atomic properties, optical beam waists and powers being fixed by measured and tabulated values.

Figure 8 showcases our ability to reliably simulate spectrograms for both type-I and type-II ladders.

Discussion

The immense success of atomic clocks relies on the fact that the transition frequency between unperturbed quantized atomic states remains completely identical from atom to atom³⁵. This ensures quantum-enabled accuracy for cesium clocks at either end of the world ticking at exactly the same rate. In a similar quantum-metrological vein, Rydberg electrometry also aims at capitalising on atomic immutability and dynamics governed by quantum mechanics. As highlighted by Ref. 12, it can quantify an electric field in SI-units from a frequency measurement, fundamental constants, and fixed, known atomic properties.

For an ideal four-level ladder system, the AT-splitting that emerges in the EIT spectrum is directly proportional

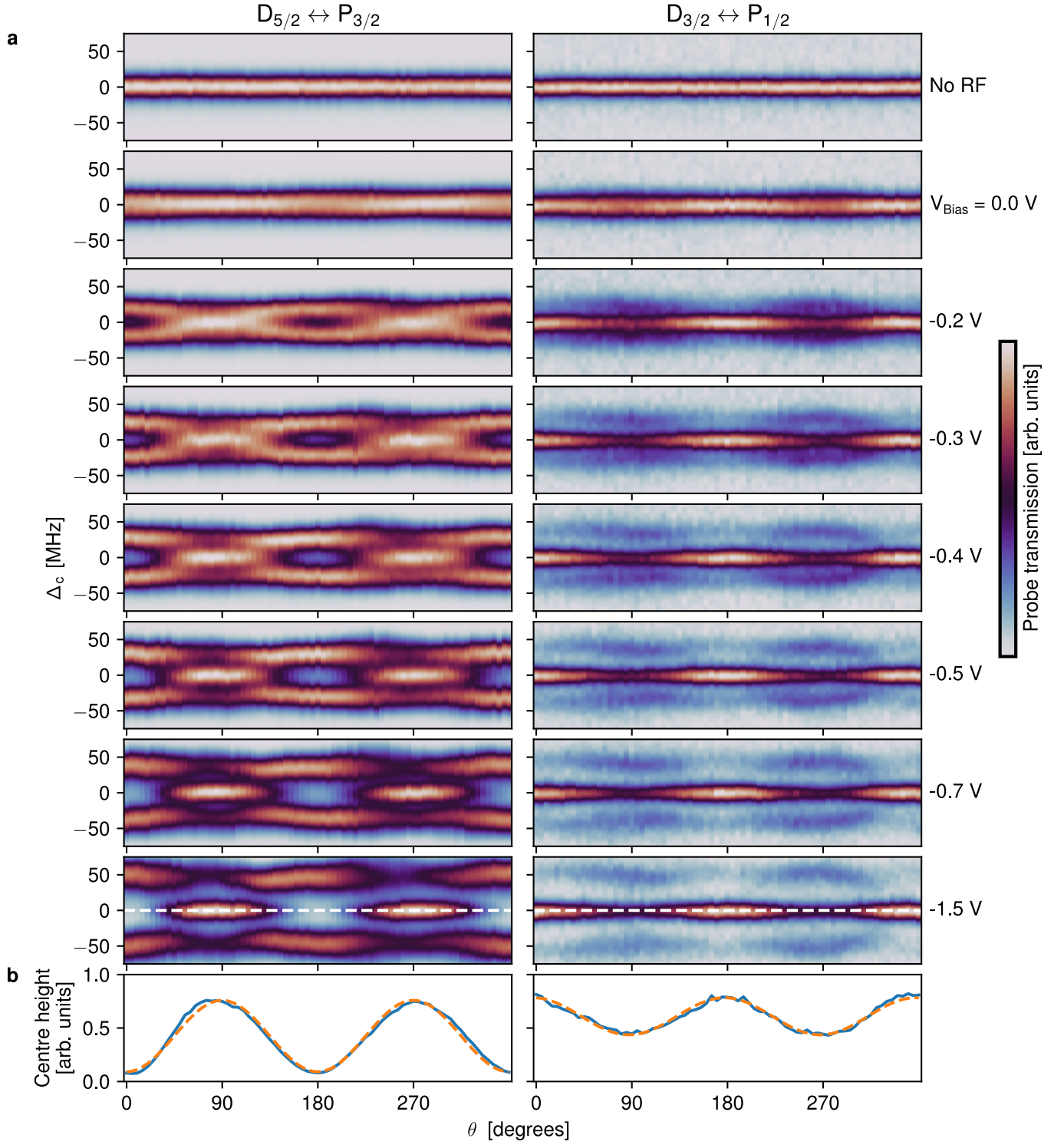


Fig. 7 | **a** Spectrograms from EIT-probing the RF-dressed $34D_{5/2} \leftrightarrow 35P_{3/2}$ (left column) and $35D_{3/2} \leftrightarrow 36P_{1/2}$ (right column) transitions. The transmission of the probe field is measured on a parameter space spanned by the RF-polarization angle θ and the coupling laser detuning Δ_c (cf. Fig. 6). From the top row, which is a reference spectrogram with no applied RF-field, moving down the RF-power increases; the RF-power shows an monotonous albeit nonlinear dependence with the bias voltage V_{Bias} of the photomixing antenna. **b** Transmitted probe light on the $\Delta_c = 0$ axis of the $V_{\text{Bias}} = -1.5$ V spectrograms as a function θ with as a function of θ_{MW} (blue lines); sinusoidal fits shown as dashed orange lines.

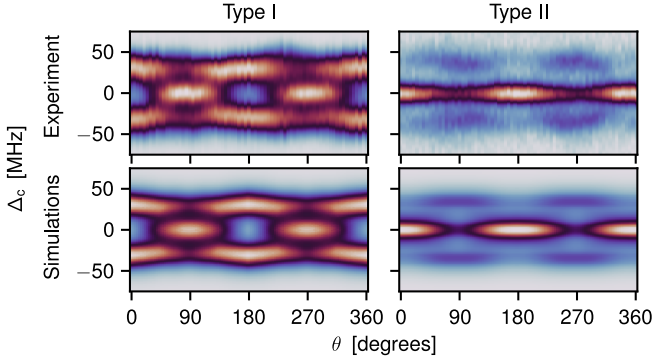


Fig. 8 | Simulated spectrograms (bottom row) for type-I (left column) and type-II ladders (right column). The corresponding experimental measurements ($V_{\text{Bias}} = -0.5$ V) are shown for comparison (top row).

to the amplitude of the RF-field dressing the topmost two Rydberg states and the constant of proportionality is given by a combination of fundamental constants and the transition dipole moment between the Rydberg states. Because of the quasi-one-electron character of Rydberg atoms, the latter can be calculated to a very

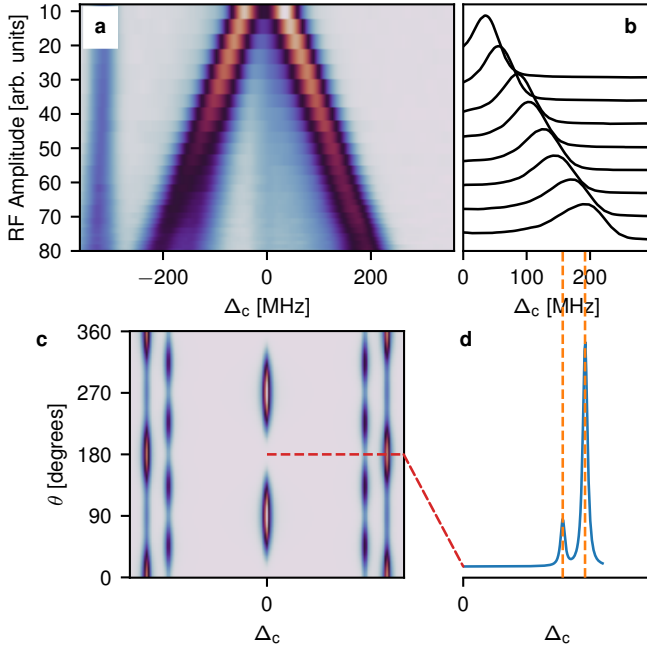


Fig. 9 | Electrometry using a type-I system with co-polarized fields. **a** Experimentally observed AT splitting of the $34D_{5/2}$ level centred on $\Delta_c = 0$. The feature at $\Delta_c \sim -306$ MHz is the $34D_{3/2}$ level (cf. Fig. 6c). Interaction with this state influences the $\Delta_c < 0$ AT peak. **b** Development in the $\Delta_c > 0$ AT peak with RF power increasing (top to bottom) from 10 to 80 (arb. units) in uniform steps. **c** Simulated spectrogram of the probe field transmission with Doppler broadening excluded. **d** Simulated probe field transmission for co-polarized fields when of Doppler broadening is absent.

high accuracy. Early work, including Ref. 12, however, has introduced the misconception that for a type-I ladder with linear co-polarized fields, one is dealing with a single transition dipole moment between r_1 and r_2 , and this has been reiterated pervasively in the literature^{14,36–46}. In fact, two transition dipole moments are in play differing by a factor of $\sqrt{2/3} \approx 0.8$ (cf. Fig. 4a) and, as noted in our above analysis, one will not be measuring a pure AT-doublet but a four-peaked spectrum. We illustrate this effect in Fig. 9a which presents the development in AT splitting when moving our RF emitter up close (~ 2 cm) to the vapor cell (see Methods). Figure 9a shows how the blue-detuned split-out peak becomes lopsided (see Fig. 9b) for high RF-powers. If the goal is to establish an accurate electrometry standard based on a type-I ladder system, the four-peak nature should be accounted for because the splitting of each pair of doublets tunes at different rates. This will skew the results if an unresolved four-peak spectrum is interpreted as a pure doublet. Figure 9c shows a simulated spectrogram for a type-I system with Doppler broadening turned off from which Fig. 9d picks out the spectrum for parallel fields that underpins the skewing of the high power trace in Figure 9b. The spectrogram Fig. 9c also elucidates that for linearly-polarized fields, the eigen-energy corresponding to a split-out peak does not change with θ . While the position of a peak remains fixed, its prominence in the spectrum will however generally change. For two overlapping broadened peaks, this may give the appearance of single feature that moves continuously as θ changes. This effect can be observed for the side-lobes in the type-I column of Fig. 8.

To be clear, it is incorrect to talk about “the” dipole moment between, say, $D_{5/2}$ and $P_{3/2}$ for a linearly-polarized coupling field^{41,42,46} because it depends on whether $m_J = |1/2|$ or $m_J = |3/2|$. It is also incorrect to resort to using the $m_J = |1/2|$ value^{37,38,44}, based on a rationale of all fields being π -polarized. This would be applicable in the absence of hyperfine structure of the ground state (see Fig. 10a,b), in which case the system is described by two parallel ideal four-state systems. For an atom in a specific, resolved hyperfine state we are, however, not dealing with parallel four-state systems, even when driving with co-polarized fields. This is evident from the diagrams in Figs. 2b and 3: moving up from any m_F -state of the ground level one counts more than three arrows. Moreover, a vertical cascade corresponding to a given m_F (Fig. 10c shows the example of $m_F = 1$ from Fig. 2b) cannot be broken down into individual “unique contributions” (cf. Fig. 10d) as was recently stated in Ref. 47. The claim of Ref. 47 that the EIT scheme acts to probe the states of r_1 individually is invalidated by the fact that these states are degenerate and therefore indirectly coupled with each other by the RF-field via the states of r_2 . Instead, to find the splittings of the system probed by EIT one needs to diagonalize the entire 7×7 matrix that describes the resonant RF interactions between the hyperfine states of r_1 and r_2 . The result of

this procedure is illustrated in Fig. 10e, replicating the dressed energies encountered Fig. 4c based on treatment in the fine structure basis.

The insight that the co-polarized cases of Figs. 2b and 3 are not represented by a collection of four-level systems means that there is *a priori* no reason why they should give rise to simple AT doublets. Indeed, as we have shown, the type-II system features a prominent central peak in its spectrum. Interestingly, the two sidelobes of the type-II triplet tunes as an ideal AT doublet with RF power with a tuning rate described by a single transition matrix element. The perfect absence of a central peak of the $\theta = 0^\circ$ type-I system in Fig. 2b can be interpreted as a destructive interference between the multiple parallel pathways represented by (2). Regardless, the spectrum does not represent a simple AT doublet.

Our recorded polarization spectrograms in Fig. 7 for type-I and type-II ladders make the complementary response of these two systems compellingly clear. In particular, their transmissions recorded as a function of θ for $\Delta_c = 0$ display out-of-phase oscillations reminiscent of the powers transmitted by and reflected off an optical polarization beam splitter. Unfortunately, because the type-II oscillation rides on a significant offset, the two “output ports” of our Rydberg atomic sensor do not serve to establish a general balanced polarimeter⁴⁸ that would offer an absolute determination of θ from measurements at a single angle. We note, however, that for sufficiently high RF powers, the $\Delta_c = 0$ angular transmission traces become invariant and either port offers an absolute determination of angle through a comparison with the EIT transmission in absence of an applied RF field.

In the current study we have focused on the case of linearly-polarized optical and RF fields and shown that either of the two complementary spectroscopic signatures for type-I and -II ladders could serve to determine the angle of polarization for the RF field. The simultaneous high fidelity of our density matrix simulations for these complementary test cases instils confidence in our simulation framework’s ability to synthesize the probe light transmission for more complex combinations of polarization states. In the future we plan to pursue the determination of arbitrary polarization states of the incoming RF field through machine learning approaches where the polarization states of probe and coupling light are varied to acquire a sequence of spectrograms. For this purpose the data diversity⁴⁹ provided by the profoundly different response from type-I and type-II may provide a significant advantage. This would open up a new paradigm for quantum-metrological⁵⁰ polarimeters that at its heart is enabled by the quantisation of atomic angular momentum.

Methods

EIT spectroscopy

All calculations of transition frequencies were performed using ARC⁵¹. The coupling laser was calibrated by scanning its frequency ~ 500 MHz across the transitions from $P_{3/2}(F=3)$ to the $nD_{3/2}$ and $nD_{5/2}$ Rydberg states generating two EIT

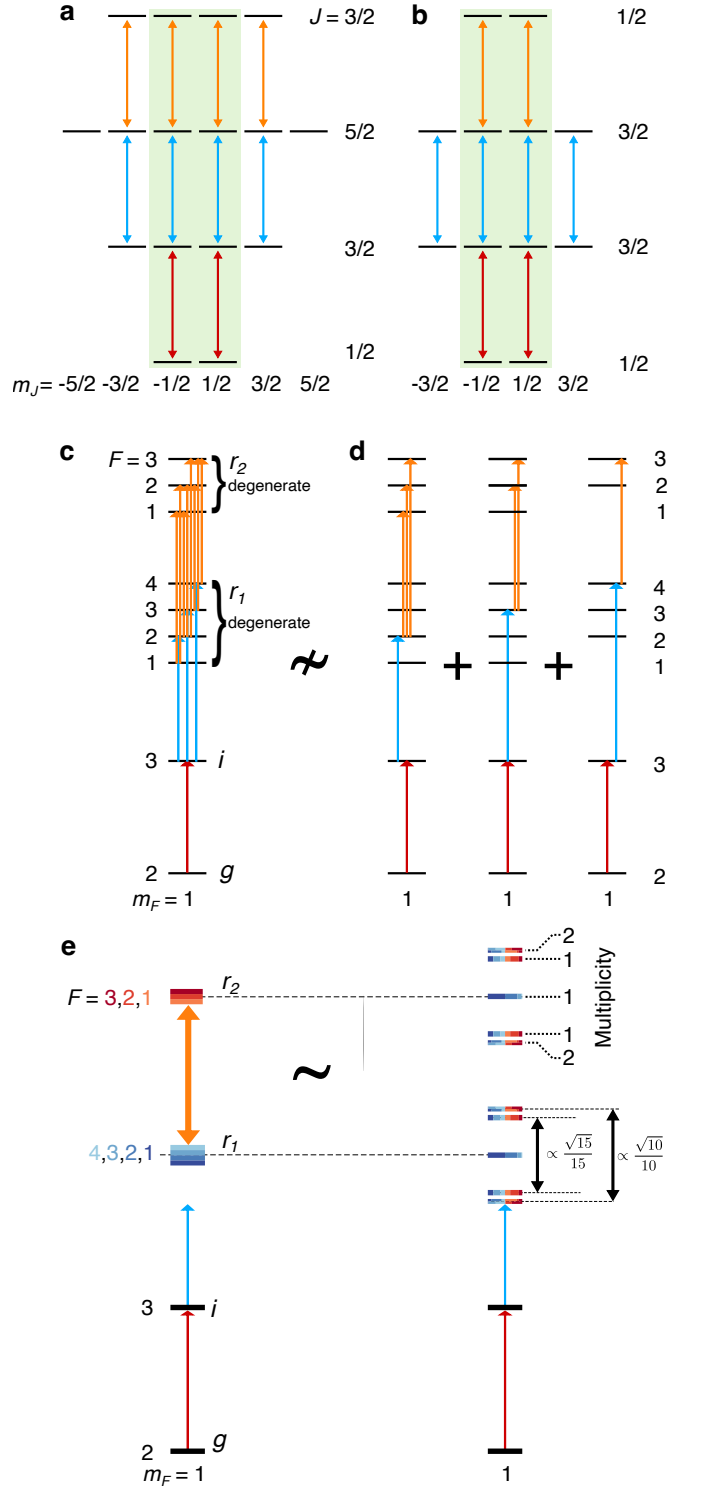


Fig. 10 | Level diagrams for a $J = \frac{1}{2} \frac{3}{2} \frac{5}{2} \frac{3}{2}$ system (a) and a $J = \frac{1}{2} \frac{3}{2} \frac{5}{2} \frac{3}{2}$ system (b) driven by π -transitions. Both realise two parallel ideal four level ladders (green background). c $m_F = 1$ ladder of Fig. 2b in isolation. The system cannot be broken down into parts as shown in d. e Level splittings obtained from the diagonalizing the matrix describing the RF-coupling (orange arrow) amongst the F -states of the Rydberg levels r_1 and r_2 when $m_F = 1$. The different F -parts of r_1 and r_2 have been colour-coded to visualise their contributions to each hybridized dressed state. The diagonalization for the $m_F=1$ ladder yields five eigen-energies with separations and multiplicities as annotated.

peaks; here $n = 34$ or $n = 35$ cf. Fig. 6c. The probe and coupling beam powers were 0.5 mW and 300 mW respectively, and their $1/e^2$ -diameters were 2.0 mm and 1.9 mm. To enable lock-in detection, the amplitude of the coupling beam was modulated at 10 kHz with an optical chopper. Probe and coupling beams were both linearly polarized in the horizontal plane after passing through polarizing beam splitter cubes and entered the vapour cell in a counter-propagating configuration to suppress Doppler broadening.

RF dressing field

The ~ 55 GHz RF field dressing our Rydberg atoms was produced by a photomixing antenna (Toptica TeraBeam 1550). Two ~ 1550 nm fiber-coupled DFB lasers are combined to produce a beatnote with frequency f_{RF} on an InGaAs photoconductive chip mounted on a bowtie-shaped antenna. The photomixing process produces linearly-polarized radiation at f_{RF} , which is collimated to a beam diverging at 12° by a silicon lens. The frequencies of the DFB lasers are temperature tuned, allowing us to target the $34D_{5/2} \leftrightarrow 35P_{3/2}$ and $35D_{3/2} \leftrightarrow 36P_{1/2}$ transitions at 56.714 GHz and 53.840 GHz respectively. The emitter is positioned 15 cm above the vapour cell which is mounted on a wooden post to minimise metallic interference.

For the measurements presented in Figure 9b,c the emitter was positioned very close (< 2 cm) to the cell. A 0.75 mm pitch wire grid polarizer was mounted in between the emitter and the cell to suppress effects a complex RF field polarization²² and ensure a linear polarization at the position of the atoms.

Density matrix calculations

Polarization spectrograms (cf. Fig. 9) are simulated with QuTiP⁵² by finding the steady-state atomic density matrix, ρ_{ss} , under the combined action of the three fields; RF, coupling (c), and probe (p). The evolution of the density matrix, ρ , is governed by the Lindblad master equation⁵³,

$$\dot{\rho} = \frac{1}{i\hbar} [H, \rho] + \sum_k \frac{\gamma_k}{2} \left(2L_k \rho L_k^\dagger - \{L_k^\dagger L_k, \rho\} \right). \quad (5)$$

The atomic Hamiltonian, H , in the dipole and rotating-wave approximations⁵⁴, takes the block form,

$$H = \frac{\hbar}{2} \begin{bmatrix} 0 & \Omega_p & 0 & 0 \\ \Omega_p^* & 2\delta_p & \Omega_c & 0 \\ 0 & \Omega_c^* & 2(\delta_p + \delta_c) & \Omega_{\text{RF}} \\ 0 & 0 & \Omega_{\text{RF}}^* & 2(\delta_p + \delta_c + \delta_{\text{RF}}) \end{bmatrix}. \quad (6)$$

Here the polarizations and Rabi frequencies of the probe, coupling and RF fields are encoded in the coupling operators Ω_k between manifolds, represented in (6) using an ordered basis of the g , i , r_1 and r_2 levels. The detuning blocks δ_k are scalar matrices because the individual states acted on by each block are not resolved. The problem is described in the $|Fm_F\rangle$ basis, to deal with the fact that the probe laser field resolves transitions between hyperfine states. The second, dissipative term of (5) is composed of collapse operators L_i with corresponding decay rates γ_i . A representation of L_i for radiative decay in the $|Fm_F\rangle$ basis is given in Supplementary Note 2. This term facilitates the inclusion of two classes of state decay: spontaneous emission, which has an operator for each possible polarization of the radiated photon, and incoherent decay, which is modelled with an auxiliary “dummy state”³⁴. Incoherent decay includes transit-time broadening and collisional

broadening of all states, but it also describes the radiative decay of the Rydberg states, which usually involves the emission of multiple photons on a decay path outside the state space of the simulation. The “dummy state” then decays rapidly, with equal probability, to each sublevel of the ground-state manifold.

Unlike Ref. 34 which time-evolved the system’s Master equation from an equally-populated ground-state manifold, we directly solve for the steady state of the system. This entails finding the non-trivial zero of the Liouvillian superoperator \mathcal{L} by recasting the density matrix as a vector (“vec-ing”)^{55,56}, and solving the equation $\dot{\rho}_{\text{ss}} = \mathcal{L}\rho_{\text{ss}} = 0$, using standard linear algebra techniques.

While the counter-propagating arrangement of coupling and probe beams compensates for a majority of the Doppler effect, we include the residual Doppler broadening of the room-temperature vapor by performing simulations with detunings that correspond to a range of atomic velocities along the probe/coupling beams, and averaging them according to the Maxwell-Boltzmann distribution. Our lock-in detection scheme is accounted for by removing a constant offset in the simulation: the resonant extinction of the probe beam without the coupling field.

REFERENCES

- [1] Adams, C. S., Pritchard, J. D. & Shaffer, J. P. Rydberg atom quantum technologies. *J. Phys. B* **53**, 012002 (2019).
- [2] Jaksch, D., Cirac, J. I., Zoller, P., Rolston, S. L., Côté, R. & Lukin, M. D. Fast quantum gates for neutral atoms. *Phys. Rev. Lett.* **85**, 2208–2211 (2000).
- [3] Bluvstein, D. *et al.* Logical quantum processor based on reconfigurable atom arrays. *Nature* **626**, 58–65 (2024).
- [4] Anderson, D. A., Sapiro, R. E. & Raithel, G. Rydberg atoms for radio-frequency communications and sensing: Atomic receivers for pulsed RF field and phase detection. *IEEE Aerosp. Electron. Syst. Mag.* **35**, 48–56 (2020).
- [5] Fancher, C. T., Scherer, D. R., John, M. C. S. & Marlow, B. L. S. Rydberg atom electric field sensors for communications and sensing. *IEEE Trans. Quantum. Eng.* **2**, 1–13 (2021).
- [6] Simons, M. T., Artusio-Glimpse, A. B., Robinson, A. K., Prajapati, N. & Holloway, C. L. Rydberg atom-based sensors for radio-frequency electric field metrology, sensing, and communications. *Meas.: Sens.* **18**, 100273 (2021).
- [7] Yuan, J., Yang, W., Jing, M., Zhang, H., Jiao, Y., Li, W., Zhang, L., Xiao, L. & Jia, S. Quantum sensing of microwave electric fields based on rydberg atoms. *Rep. Progr. Phys.* **86**, 106001 (2023).
- [8] Zhang, H., Ma, Y., Liao, K., Yang, W., Liu, Z., Ding, D., Yan, H., Li, W. & Zhang, L. Rydberg atom electric field sensing for metrology, communication and hybrid quantum systems. *Sci. Bull.* **69**, 1515–1535 (2024).
- [9] Sedlacek, J., Schwettmann, A., Kübler, H., Löw, R., Pfau, T. & Shaffer, J. Microwave electrometry with Rydberg atoms in a vapour cell using bright atomic resonances. *Nat. Phys.* **8**, 819–824 (2012).
- [10] Anderson, D. A., Sapiro, R. E. & Raithel, G. A self-calibrated SI-traceable Rydberg atom-based radio fre-

- quency electric field probe and measurement instrument. *IEEE Trans. Antennas Propag.* **69**, 5931–5941 (2021).
- [11] Otto, J. S., Chilcott, M., Deb, A. B. & Kjærgaard, N. Distant RF field sensing with a passive Rydberg-atomic transducer. *Appl. Phys. Lett.* **123**, 144003 (2023).
 - [12] Holloway, C. L., Gordon, J. A., Jefferts, S., Schwarzkopf, A., Anderson, D. A., Miller, S. A., Thaicharoen, N. & Raithel, G. Broadband Rydberg atom-based electric-field probe for SI-traceable, self-calibrated measurements. *IEEE Trans. Antennas Propag.* **62**, 6169–6182 (2014).
 - [13] Schmidt, M., Bohaichuk, S., Venu, V., Christaller, F., Liu, C., Ripka, F., Kübler, H. & Shaffer, J. P. Rydberg-atom-based radio-frequency sensors: amplitude-regime sensing. *Opt. Express* **32**, 27768 (2024).
 - [14] Jing, M., Hu, Y., Ma, J., Zhang, H., Zhang, L., Xiao, L. & Jia, S. Atomic superheterodyne receiver based on microwave-dressed Rydberg spectroscopy. *Nat. Phys.* **16**, 911–915 (2020).
 - [15] Otto, J. S., Hunter, M. K., Kjærgaard, N. & Deb, A. B. Data capacity scaling of a distributed Rydberg atomic receiver array. *J. Appl. Phys.* **129**, 154503 (2021).
 - [16] Cui, Y. *et al.* Extending bandwidth sensitivity of Rydberg-atom-based microwave electrometry using an auxiliary microwave field. *Phys. Rev. A* **107**, 043102 (2023).
 - [17] Liu, B., Zhang, L.-H., Liu, Z.-K., Zhang, Z.-Y., Zhu, Z.-H., Gao, W., Guo, G.-C., Ding, D.-S. & Shi, B.-S. Highly sensitive measurement of a megahertz rf electric field with a rydberg-atom sensor. *Phys. Rev. Appl.* **18**, 014045 (2022).
 - [18] Mathis, H. F. A short proof that an isotropic antenna is impossible. *Proc. Inst. Radio Eng.* **39**, 970–970 (1951).
 - [19] Mathis, H. F. On isotropic antennas. *Proc. Inst. Radio Eng.* **42**, 1810–1810 (1954).
 - [20] Scott, W. & Hoo, K. A theorem on the polarization of null-free antennas. *IEEE Trans. Antennas Propag.* **14**, 587–590 (1966).
 - [21] Cloutman, M., Chilcott, M., Elliott, A., Otto, J. S., Deb, A. B. & Kjærgaard, N. Polarization-insensitive microwave electrometry using Rydberg atoms. *Phys. Rev. Appl.* **21**, 044025 (2024).
 - [22] Chopinaud, A. & Pritchard, J. Erratum: Optimal State choice for Rydberg-atom microwave sensors [Phys. Rev. Appl. 16 , 024008 (2021)]. *Phys. Rev. Appl.* **22**, 029902 (2024).
 - [23] Yuan, S., Jing, M., Zhang, H., Zhang, L., Xiao, L. & Jia, S. Isotropic antenna based on Rydberg atoms. *Opt. Express* **32**, 8379–8388 (2024).
 - [24] Sedlacek, J. A., Schwettmann, A., Kübler, H. & Shaffer, J. P. Atom-based vector microwave electrometry using rubidium rydberg atoms in a vapor cell. *Phys. Rev. Lett.* **111**, 063001 (2013).
 - [25] Jiao, Y., Hao, L., Han, X., Bai, S., Raithel, G., Zhao, J. & Jia, S. Atom-based radio-frequency field calibration and polarization measurement using cesium nDJ Floquet states. *Phys. Rev. Appl.* **8**, 014028 (2017).
 - [26] Wang, Y. *et al.* Precise measurement of microwave polarization using a Rydberg atom-based mixer. *Opt. Express* **31**, 10449–10457 (2023).
 - [27] Elgee, P. K., Cox, K. C., Hill, J. C., Kunz, P. D. & Meyer, D. H. Complete three-dimensional vector polarimetry with a Rydberg-atom rf electrometer. *Phys. Rev. Appl.* **22**, 064012 (2024).
 - [28] Borówka, S., Krokosz, W., Mazelanik, M., Wasilewski, W. & Parniak, M. Rydberg-atom-based system for benchmarking millimeter-wave automotive radar chips. *Phys. Rev. Appl.* **22**, 034067 (2024).
 - [29] Fleischhauer, M., Imamoglu, A. & Marangos, J. P. Electromagnetically induced transparency: Optics in coherent media. *Rev. Mod. Phys.* **77**, 633–673 (2005).
 - [30] Cohen-Tannoudji, C. N. The Autler-Townes Effect Revisited. in *Amazing Light* (Springer New York, 1996) pp. 109–123.
 - [31] Our diagram (Fig. 2a) includes six dipole-allowed transitions from the $D_{5/2}(F = 1, m_F = 0, \pm 1)$ states that are omitted in Ref. 24 and also are also in the reproduction of the diagram in Ref. 32.
 - [32] Schlossberger, N., Prajapati, N., Berweger, S., Rotunno, A. P., Artusio-Glimpse, A. B., Simons, M. T., Sheikh, A. A., Norrgard, E. B., Eckel, S. P. & Holloway, C. L. Rydberg states of alkali atoms in atomic vapour as SI-traceable field probes and communications receivers. *Nat. Rev. Phys.* **6**, 606–620 (2024).
 - [33] A general rule for the number of spectral peaks is given in Ref. 21.
 - [34] Sedlacek, J. *Microwave and Surface Electrometry with Rydberg Atoms* Ph.D. thesis University of Oklahoma (2016).
 - [35] Lombardi, M. A., Heavner, T. P. & Jefferts, S. R. NIST primary frequency standards and the realization of the SI second. *NCSLI Measure* **2**, 74–89 (2007).
 - [36] Simons, M. T., Gordon, J. A., Holloway, C. L., Anderson, D. A., Miller, S. A. & Raithel, G. Using frequency detuning to improve the sensitivity of electric field measurements via electromagnetically induced transparency and Autler-Townes splitting in Rydberg atoms. *Appl. Phys. Lett.* **108**, 174101 (2016).
 - [37] Simons, M. T., Gordon, J. A. & Holloway, C. L. Simultaneous use of Cs and Rb Rydberg atoms for dipole moment assessment and RF electric field measurements via electromagnetically induced transparency. *J. Appl. Phys.* **120**, 123103 (2016).
 - [38] Holloway, C. L., Simons, M. T., Gordon, J. A., Wilson, P. F., Cooke, C. M., Anderson, D. A. & Raithel, G. Atom-based RF electric field metrology: From self-calibrated measurements to subwavelength and near-field imaging. *IEEE Trans. Electromagn. Compat.* **59**, 717–728 (2017).
 - [39] Zhang, L., Jia, Y., Jing, M., Guo, L., Zhang, H., Xiao, L. & Jia, S. Detuning radio-frequency electrometry using Rydberg atoms in a room-temperature vapor cell. *Laser Physics* **29**, 035701 (2019).
 - [40] Monika, Rawat, H. S. & Dubey, S. K. RF E-field sensing using Rydberg atom-based microwave electrometry. *MAPAN* **35**, 555–562 (2020).
 - [41] Meyer, D. H., O’Brien, C., Fahey, D. P., Cox, K. C. & Kunz, P. D. Optimal atomic quantum sensing using electromagnetically-induced-transparency readout. *Phys. Rev. A* **104**, 043103 (2021).
 - [42] Zhao, R., Feng, M., Zhu, J., Li, Z., Zheng, J., Ma, Z., Shi, Y., Tang, J. & Liu, J. Toward the measurement of microwave electric field using cesium vapor MEMS cell. *IEEE Electron Device Lett.* **44**, 2031–2034 (2023).
 - [43] Bussey, L. W., Kale, Y. B., Winter, S., Burton, F. A., Lien, Y.-H., Bongs, K. & Constantinou, C. Numerical model of n-level cascade systems for atomic radio frequency sensing applications. *EPJ Quantum Technol.* **11**, 77 (2024).

- [44] Yang, B., Yan, Y., Li, X., Zhao, H., Xiao, L., Li, X., Deng, J. & Cheng, H. Sensitivity of Rydberg microwave electrometry limited by laser frequency noise. *Phys. Rev. A* **109**, 032609 (2024).
- [45] Wu, Y., Xiao, D., Zhang, H. & Yan, S. Optimization strategies for operational parameters of Rydberg atom-based amplitude modulation receiver. *Chin. Phys. B* **34**, 013201 (2025).
- [46] Feng, Z., Liu, X., Song, Z. & Qu, J. Multi-parameter microwave quantum sensing with a single atomic probe. *Sci. Rep.* **15**, 5379 (2025).
- [47] Schlossberger, N., Prajapati, N., Artusio-Glimpse, A. B., Berweger, S., Simons, M. T., Watterson, W. J., Shylla, D. & Holloway, C. L. Calibration of Autler-Townes based electrometry in Rydberg states of alkali atoms. in *2024 Conference on Precision Electromagnetic Measurements (CPEM)* (IEEE, 2024) pp. 1–2.
- [48] Patterson, L. H. C., Kihlstrom, K. E. & Everest, M. A. Balanced polarimeter: A cost-effective approach for measuring the polarization of light. *Am. J. Phys.* **83**, 91–94 (2015).
- [49] Gong, Z., Zhong, P. & Hu, W. Diversity in machine learning. *IEEE Access* **7**, 64323–64350 (2019).
- [50] Nawrocki, W. *Introduction to Quantum Metrology: The Revised SI System and Quantum Standards* (Springer International Publishing, 2019).
- [51] Šibalić, N., Pritchard, J., Adams, C. & Weatherill, K. ARC: An open-source library for calculating properties of alkali Rydberg atoms. *Comput. Phys. Commun.* **220**, 319–331 (2017).
- [52] Johansson, J., Nation, P. & Nori, F. QuTiP 2: A Python framework for the dynamics of open quantum systems. *Comput. Phys. Commun.* **184**, 1234–1240 (2013).
- [53] Breuer, H.-P. & Petruccione, F. *The Theory of Open Quantum Systems* (Oxford University Press, 2007).
- [54] Berman, P. R. & Malinovsky, V. S. *Principles of Laser Spectroscopy and Quantum Optics* (Princeton University Press, Princeton, 2011).
- [55] Am-Shallem, M., Levy, A., Schaefer, I. & Kosloff, R. Three approaches for representing Lindblad dynamics by a matrix-vector notation. (2015) arXiv:1510.08634 [quant-ph].
- [56] Schlimgen, A. W., Head-Marsden, K., Sager, L. M., Narang, P. & Mazziotti, D. A. Quantum simulation of the Lindblad equation using a unitary decomposition of operators. *Phys. Rev. Res.* **4**, 023216 (2022).
- [57] Sobelman, I. I. *Atomic Spectra and Radiative Transitions* (Springer Berlin Heidelberg, 1992).
- [58] Varshalovich, D. A., Moskalev, A. N. & Khersonskii, V. K. *Quantum Theory of Angular Momentum* (World Scientific, 1988).
- [59] Metcalf, H. J. & van der Straten, P. *Laser Cooling and Trapping* (Springer New York, 1999).
- [60] Auziņš, M., Budker, D. & Rochester, S. M. *Optically polarized atoms* (Oxford University Press, Oxford, 2014).
- [61] Shimoda, K. Line broadening and narrowing effects. in *High-Resolution Laser Spectroscopy* edited by Shimoda, K. (Springer Berlin Heidelberg, Berlin, Heidelberg, 1976) pp. 11–49.
- [62] Thomas, J. E. & Quivers, W. W. Transit-time effects in optically pumped coupled three-level systems. *Phys. Rev. A* **22**, 2115–2121 (1980)

Acknowledgments

This work was supported by the Marsden Fund of New Zealand (Contracts No. UOO1923 and UOO1729) and by MBIE (Contract No. UOOX1915). We thank J. Shaffer and S. Hofferberth for their input on density matrix calculations. N.K. thanks Mikkel Andersen for discussions.

Author contributions

N.K. conceived and supervised the project; M.Cloutman performed experiments with support from M.Chilcott, A.B.D., and S.O.; M.Cloutman analysed the data with support from M.Chilcott; M.Chilcott and A.E. carried out density matrix calculations; N.K., M.Cloutman, and M.Chilcott wrote the manuscript with input from all authors.

Competing interests

The authors declare no competing financial interests.

Additional information

Supplementary Information accompanies this paper.

Correspondence should be addressed to Niels Kjærgaard.

SUPPLEMENTARY NOTE 1

Coupling from a state of the intermediate level to a dressed Rydberg state

To arrive at (2) we must evaluate $\left| \sum_{F=1}^4 C_{Jm_JIm_I}^{Fm_F} \langle F'm'_F | r_0 | Fm_F \rangle \right|^2$.

Using the Wigner Eckart theorem we have

$$\sum_{F=1}^4 C_{Jm_JIm_I}^{Fm_F} \langle F'm'_F | r_0 | Fm_F \rangle = \sum_{F=1}^4 C_{Jm_JIm_I}^{Fm_F} C_{Fm_F10}^{F'm'_F} (2F'+1)^{-\frac{1}{2}} \langle F' || r_0 || F \rangle \quad (S1)$$

$$\stackrel{\text{Ref. 57 p.84}}{=} \sum_{F=1}^4 C_{Jm_JIm_I}^{Fm_F} C_{Fm_F10}^{F'm'_F} (2F'+1)^{-\frac{1}{2}} (-1)^{J'+I+F+1} \sqrt{(2F'+1)(2F+1)} \begin{Bmatrix} J' & F' & I \\ F & J & 1 \end{Bmatrix} \langle J' || r_0 || J \rangle \quad (S2)$$

$$= (-1)^{J'+I+F'+1} \sqrt{2F'+1} \langle J' || r_0 || J \rangle \sum_{F=1}^4 C_{Jm_JIm_I}^{Fm_F} C_{F'm'_F10}^{Fm_F} \begin{Bmatrix} J' & F' & I \\ F & J & 1 \end{Bmatrix} \quad (S3)$$

$$\stackrel{\text{Ref. 58 p.261}}{=} (-1)^{J'+I+F'+1} \sqrt{2F'+1} \langle J' || r_0 || J \rangle C_{J'-m_JF'm'_F}^{Im_I} C_{J'-m_JJm_J}^{10}, \quad (S4)$$

from which it follows that

$$\left| \sum_{F=1}^4 C_{Jm_JIm_I}^{Fm_F} \langle F'm'_F | r_0 | Fm_F \rangle \right|^2 \propto \begin{pmatrix} J' & J & 1 \\ -m_J & m_J & 0 \end{pmatrix}^2 \begin{pmatrix} J' & F' & I \\ -m_J & m'_F & m_J - m'_F \end{pmatrix}^2. \quad (S5)$$

SUPPLEMENTARY NOTE 2

In this supplement, we provide additional details on computing the density matrix, and connecting it to experimental observations. In particular, we include the matrix form of the operators necessary to formulate the master equation (5), expanded over the hyperfine $|Fm_F\rangle$ basis.

Probe extinction

As discussed in the main text, the extinction of the probe beam through an atomic vapour follows the Beer-Lambert law, (4). The extinction coefficient α for a vapour of density n at a transition of frequency ω_p is composed of off-diagonal elements of the atomic density matrix ρ ³⁴,

$$\alpha = \frac{2n\omega_p}{c\epsilon_0\hbar} \sum_{g_l \in g, i_m \in i} |\vec{\mu}_{i_m g_l}|^2 \text{Im} \left(\frac{\rho_{g_l i_m}}{\Omega_{i_m g_l}} \right), \quad (S6)$$

with the sum running over the states of the g - and i -level manifolds. The inter-state couplings $\Omega_{i_m g_l}$, and dipole moments $\vec{\mu}_{i_m g_l}$ of (S6) are expressed below.

As described in the methods section, the density matrix is governed by the master equation of (5), with the atomic Hamiltonian (6).

Field-induced Couplings

The coupling operators Ω_k for each transition take the usual form of the Rabi frequency,

$$\Omega_k = -\frac{\vec{\mu}_k \cdot \vec{E}_k}{\hbar}, \quad (S7)$$

for the electric field \vec{E}_k , and transition dipole moment $\vec{\mu}_k$.

For convenience, we factor the coupling operators⁵⁹ into a scalar radial component $\Omega_k^{(r)}$ (the radial Rabi frequency) and an angular component, expanded over the spherical basis⁶⁰,

$$\Omega_k = \Omega_k^{(r)} \sum_{q=-1,0,1} A_k^{(q)} u_k^{(q)}. \quad (\text{S8})$$

Physically, $q = -1, 0, +1$ represents the change in angular momentum associated with σ^- , π , and σ^+ excitations, respectively. When expressed in terms of the Cartesian components of a unit vector \hat{E} along the electric field direction (i.e., $\vec{E} = |\vec{E}|\hat{E}$), the coefficients $A^{(q)}$ are given by

$$A^{(1)} = -\frac{1}{\sqrt{2}}(\hat{E}_x + i\hat{E}_y), \quad (\text{S9})$$

$$A^{(0)} = \hat{E}_z, \quad (\text{S10})$$

$$A^{(-1)} = \frac{1}{\sqrt{2}}(\hat{E}_x - i\hat{E}_y). \quad (\text{S11})$$

The elements of each matrix $u_k^{(q)}$ are found by repeated applications of the Wigner-Eckart theorem, with $\Omega_k^{(r)}$ absorbing the reduced matrix element,

$$\begin{aligned} \langle SLJFmF | u_k^{(q)} | S'L'J'F'mF' \rangle = & \\ & (-1)^{1+L'+S+J+J'+I-m'_F} \\ & \times \sqrt{(2J+1)(2J'+1)(2F+1)(2F'+1)} \\ & \times \begin{Bmatrix} L' & J' & S \\ J & L & 1 \end{Bmatrix} \times \begin{Bmatrix} J' & F' & I \\ F & J & 1 \end{Bmatrix} \\ & \times \begin{pmatrix} F & 1 & F' \\ m_F & q & -m'_F \end{pmatrix}. \end{aligned} \quad (\text{S12})$$

Decay operators

Decays that maintain coherence between states correspond to the emission of a photon via σ^+ , π , and σ^- transitions, associated with atomic angular momentum changes $q = -1, 0, 1$, respectively. A decay path between two states is described by a collapse operator, $L_k^{(q)}$, for each q , with elements

$$\begin{aligned} \langle SLJFmF | L_k^{(q)} | S'L'J'F'mF' \rangle = & \\ & (2L+1)(2J+1)(2J'+1)(2F+1)(2F'+1) \\ & \times \begin{Bmatrix} L' & J' & S \\ J & L & 1 \end{Bmatrix}^2 \times \begin{Bmatrix} J' & F' & I \\ F & J & 1 \end{Bmatrix}^2 \\ & \times \begin{pmatrix} F & 1 & F' \\ m_F & q & -m'_F \end{pmatrix}^2. \end{aligned} \quad (\text{S13})$$

The right-hand side of this equation is proportional to the squared right-hand side of (S12), with the notable feature that, for a given initial state, the sum over all q and possible jumps is unity. Thus the path's γ_k (which is shared for all q) is the total radiative lifetime for each initial state.

We treat decay from the Rydberg states as primarily incoherent. The vast majority of possible radiative decay paths pass through states outside of those included in our model. The long lifetime of the Rydberg states also means that the rates of non-radiative incoherent decay processes are of similar magnitude to the radiative decay. These include transit-time broadening and collisional broadening⁶¹. We note the rudimentary model for transit-time broadening⁶² is only valid for large beams where the decay rate is larger than the transit rate.

The incoherent decay paths are included in our model by means of a “dummy state” with no angular momentum character. Excited states decay to this dummy state via a collapse operator with a single non-zero element. In the case of the i -level states, the rate is given by the sum of the transit-time broadening and collisional broadening rates. For the two Rydberg levels, the radiative decay rate is added to this. The “dummy state” itself decays rapidly into the $|g\rangle$ manifold (with a near-infinite γ).